

The Hydrodynamics of Astrophysical jets: Scaled Experiments and Numerical Simulations

Original

The Hydrodynamics of Astrophysical jets: Scaled Experiments and Numerical Simulations / M., Belan; S., Massaglia; Tordella, Daniela; M., Mirzaei; S., de Ponte. - In: ASTRONOMY & ASTROPHYSICS. - ISSN 0004-6361. - STAMPA. - 554:(2013), pp. A99/1-9. [10.1051/0004-6361/201321040]

Availability:

This version is available at: 11583/2507765 since:

Publisher:

EDP Sciences

Published

DOI:10.1051/0004-6361/201321040

Terms of use:

This article is made available under terms and conditions as specified in the corresponding bibliographic description in the repository

Publisher copyright

(Article begins on next page)

The Hydrodynamics of Astrophysical jets: Scaled Experiments and Numerical Simulations

M. Belan¹, S. Massaglia², D. Tordella³, M. Mirzaei¹, and S. de Ponte⁴

¹ **Dipartimento di Scienze e Tecnologie Aerospaziali**, Politecnico di Milano, Italy e-mail: belan@aero.polimi.it

² Dipartimento di Fisica, Università degli Studi di Torino, via Pietro Giuria 1, 10125 Torino, Italy e-mail: silvano.massaglia@unito.it

³ **Dipartimento di Ingegneria Meccanica e Aerospaziale**, Politecnico di Torino, I e-mail: daniela.tordella@polito.it

⁴ **retired, formerly Dipartimento di Ingegneria Aerospaziale**, Politecnico di Milano, I e-mail: deponte@aero.polimi.it

Received ?? / Accepted ??

ABSTRACT

Context. In the present paper we study the propagation of hypersonic hydrodynamic jets (**Mach number greater than 5**) in a laboratory vessel and make comparisons with numerical simulations of axially symmetric flows in the same initial and boundary conditions. The astrophysical context is that of the jets issuing from Young Stellar Objects (YSOs).

Aims. In order to have a further insight into the jets from YSOs, a set of experiments and numerical simulations of hypersonic jets is performed in the range of Mach numbers from 10 to 20 and for jet-to-ambient density ratios from 0.85 to 5.4, using different gas species and observing jet lengths of the order of 150 initial radii or more. Exploiting the scalability of the hydrodynamic equations, we intend to reproduce the YSO jet behaviors as far as the jet and head velocities and elapsed times are concerned. In addition, we can make comparisons between the simulated, the experimental and the observed morphologies.

Methods. In the experiments the gas pressure and temperature are increased by a fast, quasi **isentropic** compression by means of a piston system **operating on a time scale of tens of millisecond**, while the gas density is visualized and measured by means of an electron beam system. The PLUTO software for the numerical solution of mixed hyperbolic/parabolic conservation laws targeting high Mach number flows in astrophysical fluid dynamics is used. **We consider axisymmetric initial conditions and carry out numerical simulations in cylindrical geometry.** The code has a modular flexible structure whereby different numerical algorithms can be separately combined to solve systems of conservation laws using the finite volume or finite difference approach based on Godunov-type schemes.

Results. The agreement between experiments and numerical simulations is fairly good in the majority of comparisons. The resulting scaled flow velocities and elapsed times are close to the ones shown by observations. The morphologies of the density distributions agree with the observed ones as well.

Conclusions. **The laboratory and the simulated hypersonic jets are all pressure matched, i.e. their axial regions are almost isentropic at the nozzle exit.** They maintain their collimation for long distances in terms of the initial jet radii, without including magnetic effects. This yields a qualitatively good agreement with the observed YSO jets morphologies. It remains to be seen what happens when non axially symmetric perturbations of the flow are imposed at the nozzle both in the experiment and in the simulation.

Key words. ISM/Stars: jets and outflows – MHD – Stars: pre-main sequence, formation

1. Introduction

Astrophysical jets are observed in the Universe in a large variety of environments and under a wide range of sizes and powers: in Active Galactic Nuclei (AGNs), where they are generated to travel up to a few thousands of Megaparsecs and to attain the largest powers observed in the Universe (**up to $\sim 10^{48}$ ergs s⁻¹**); in the **Giant Molecular Clouds**, emanating in the vicinities of Young Stellar Objects (YSOs), these jets reach distances of some parsecs (**Reipurth & Bally 2001**); by neutron

stars in galactic X-ray binary star systems, such as GRS 1915+105, that behave as microquasars generating relativistic jets (**Fender 2004**); in the post-AGB stars in pre-planetary and planetary nebulae; from the SS433 binary source, with precessing jets that lead to a peculiar phenomenology (**Frank 2011**); inside the Crab Nebula from an embedded pulsar, observed at X-ray energies (**Hester 2008**), and, eventually, they can be at the base of the phenomenology of Gamma Ray Bursts, observed at the highest radiation energies, that are still elusive phenomena due to their extreme distances (**Granot 2006**).

The hypersonic jets are of course also of great interest in aero- and astronautical applications, however many works are mainly focused on the jet near field, on the thrust obtained by means of jets, on jet-body interactions and other applied issues. The literature about these topics is large, from the early works of Love et al. (1959) or Ashkenas and Sherman (1966), but it is definitely hard to find experimental works about the long scale behaviour of free hypersonic jets. Often the jets are compressible but not hypersonic, or, if hypersonic, they are underexpanded (see e.g. Bulent and Volkan 2002, Belan et al. 2010). Studies on the mid-term field of nearly isentropic laboratory jets up to Mach 2 can be found only in two papers by Zaman (1998, 1999). For these reasons, this work can also help in clarify some aspects of the basic fluid dynamics of these flows.

We are witnessing, in the recent years, many experiments that try to reproduce in the laboratory at least some aspects of astrophysical phenomena. In the domain of **radiative hydrodynamics**, experiments have been carried out to understand, **from the analyses of the emitted spectra**, the physics of radiative shocks in accretion flows about young stars (Rus et al. 2002, González et al. 2009), to study the formation and evolution of **magnetized** accretion disks (Bellan et al. 2005) and to examine different aspects of the complex physics of stellar and galactic jets (Bellan et al. 2009). Considering laboratory simulations of astrophysical jets, different techniques have been employed, i.e. high-power lasers (Hartigan et al. 2009, Gregory et al. 2009, Falize et al. 2011), radial wire and foil Z-pinch (Lebedev et al. 2005, Suzuki-Vidal et al. 2010). These experiments reproduce some features of the actual YSO jets such as jet velocities, temperatures and cooling effects. Comparisons between laboratory jets produced by pulsed-power Z-pinch machines with simulations have been discussed by Ciardi et al. (2009). **The disadvantage of these techniques is the inability to produce long collimated jets, where long means orders of magnitude longer than the width of the formation region.**

Hypersonic hydrodynamic flows in a vacuum vessel have been recently studied in laboratory and by numerical means (Tordella et al. 2011, Belan et al. 2010). The hydrodynamic approach aims to highlight the *compressibility* effects, that observations show to be of the utmost importance in jets. In fact, **observational data give** clear evidence of shocked emission from structures that form at the jet's head; on the jet axis as well we observed series of aligned emission knots. **Knot formation was evident ever since the early numerical studies of astrophysical jets by Norman et al. (1982), and were interpreted as shocks originated by jet compression or velocity variations in the jet and/or by the nonlinear evolution of shear-layer instabilities (Massaglia et al. 1992, Micono et al. 2000).** These structures are particularly well studied in YSO jets, due to the rich di-

agnostics supplied by the spectral line emission, and allow to well constrain the values of the jet Mach numbers, **between 10 and 40**, and jet-to-ambient density ratios, **in the range 1–10**. It is therefore extremely interesting for us to be able to generate and study in the laboratory jets with Mach numbers and jet-to-ambient density ratios that are close to the ones inferred for YSO jets. **It is worth noticing that, while the absolute velocities of the plasma jets produced in Z-pinch machines it is fairly close to the one of the actual YSO jets, $\sim 200 \text{ km s}^{-1}$, they have densities that exceed the ambient density by orders of magnitude (Lebedev et al. 2004).**

We carry out in this paper a systematic analysis of hydrodynamic hypersonic jets, exploring the range of Mach numbers 10, 15 and 20 and different jet-to-ambient density ratios, carrying out comparisons between experimental and numerical results. The plan of the paper is the following: in Section 2 and 3 we **describe** the experimental and numerical setups, in Section 4 we **present** the results obtained, that are discussed in Section 5. Conclusions are drawn in Section 6.

2. Experimental setup

The laboratory experiment was carried out by means of facilities designed and built specifically for the generation and display of hypersonic jets. Detailed information can be found in the works by Belan et al. (2008, 2010, 2011, 2012), including descriptions of the configurations and improvements adopted in different experiments. The jets under test in this work are obtained by means of suitable de Laval nozzles and propagate along the longitudinal axis of a modular cylindrical vacuum vessel, a sample setup is shown in Fig. 1. Visualizations and measurements are based on the electron beam technique, **which is described in detail later.**

The available set of nozzles was specially designed for monoatomic gases flows, taking account of the real flow properties, including **viscous boundary layer** and heat exchange effects. **These calculations yield the momentum and temperature evolution in the viscous layer near the nozzle wall. It is here important to recall that the viscous layer undergoes an unavoidable transition to turbulence in the divergent part of the nozzle.** Each de Laval nozzle is designed for a nominal Mach number, which is obtained by imposing a given stagnation-to-ambient pressure ratio p_0/p_a in such a way as to match the jet pressure p_j at the nozzle exit and the ambient pressure p_a . Slight adjustments of the pressure ratios are possible, so that all the jets are generated under pressure matched or nearly matched conditions, i.e. the jet pressure p_j at the nozzle exit is close to the ambient pressure p_a , in the range $p_a \pm 20\%$. **This permits to produce jets with different Mach numbers by means of the same nozzle, for example the nozzle designed nominally for Mach 10 can be used to create jets in the range $7.5 < M < 12.5$, see also ta-**

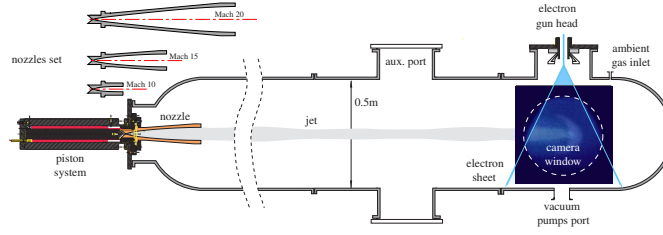


Fig. 1. Experiment setup. The total vessel length depends on the number of assembled sections. The set of de Laval nozzles used in this work is shown on the left. All the nozzles have the same converging section and throat (radius=1mm), whilst the diverging section depends on the design Mach number. The output radii r_n are 12.0, 35.7 and 60.9mm.

ble 1. Due to the boundary layer within the nozzles, the actual jet diameter is less than the diameter of the nozzle exit section. A proper definition for the reference jet diameter r_0 at the nozzle output can be given by observing that in the present experiment the information is mainly obtained from density-dependent measurements: for this reason, r_0 will be identified as the radius at which the density is reduced of 0.5 times the difference between the axial value and the minimum value at the nozzle boundary. This definition is a generalized form of the half density–half width criterion, and can be extended to the far field for any value of the density ratio, assuming as jet radius the point of half width between the central maximum and the external minimum, as shown in Fig. 2.

The jet gas is fed to the nozzles by a fast piston system purposely designed, which compresses the jet gas to stagnation pressure in the 0.1 to 0.7 MPa (1–7 bar) range. At the same time, the piston raises the gas temperature, increasing significantly the gas enthalpy. The piston is a purely mechanical system, machined at a high precision level which ensures a good repeatability to the jet production. The repeatability is high on global variables as the time variation of the mass flow and on large scale structures. It is naturally less good on fine morphological details highly dependent on the boundary conditions at the nozzle output (Tordella et al. 2011, Belan et al. 2012). In particular, the mass flow curves show that the nominal mass flow of the jet can be reached after a certain transient time elapses. All the results presented in this work are obtained by satisfying this condition, i.e. the data are only collected when the mass flow is close to the asymptotic value for given Mach number and pressure ratio p_0/p_a .

The jets under study are created inside a modular vacuum vessel, up to 5 cylindrical sections having a diameter of 0.5m are available. These can be assembled together, giving a maximum available length for the spatial evolution of the jets of about 3.3 m, corresponding at least to 150 jet radii. A set of pumps are used to lower the internal pressure, that can reach a minimum level about 0.5 – 1 Pa. Pressures inside the vessel are monitored by 0.25% accuracy transducers. The vessel diameter is much larger than the jet diameter in all tests, so the lateral walls effects are negligible and the jets can be considered as free jets until they hit the vessel’s end. The ambient pressure inside the vessel is controlled by means of a valves system

which sets the desired ambient density (at pressures in the range 1.5 to 100 Pa) using a gas in general different from the gas flowing in the jet. The use of different gases for the jet (He,Ar,Xe) and the ambient (He,Ar,Xe,air) allows to set the jet-to-ambient density ratio $\eta = \rho_j/\rho_a$ over a wide range, from underdense conditions ($\eta < 1$) to very overdense conditions ($\eta \gg 1$).

The vessel modularity gives the advantage of fitting the total length to the needs of the individual tests: in general, for the sake of studying the jets evolution over long distances, a longer size is needed to follow the development of higher Mach number jets, because of their larger diameter. Thus, the general setup depends on the nozzle in use: the main parameters, including **the matched pressure ratios, known with very good accuracy, as well as reference lengths and domain lengths**, are listed in Table 1. **The vessel lengths vary depending on the sections number and on the nozzle length.**

Visualizations and measurements are based on the electron beam method, thanks to an electron gun specifically designed and built in the laboratory. **Detailed descriptions of this method, well known in experimental fluid mechanics, can be found in Muntz (1968) and Bütetfisch and Vennemann (1974).** The device is equipped with a deflection system to create an electron sheet, adjustable up to 2 mA at 20 kV. **It is operated in continuous mode, i.e. it is turned on before the piston start and switched off at the end of the experiment. However, due to the high speed of the jets, the total working time of the electron gun is of the order of few seconds for each test. The power of the beam is easily obtained as the current–voltage product: in a typical test the electron gun is not used at the maximum power, usually a power of $1\text{mA} \times 16\text{kV} = 16\text{W}$ can be assumed as a reference. This value can be compared to the power of the jets to estimate the perturbation due to the measurement method. It turns out that the beam-to-jet power or energy ratio is typically of the order of 1/200 or better.**

The electron sheet intercepts the jet under test and generates a plane fluorescent section of the flow, shown from above in Fig. 1. These 2-D sections are then acquired as digital images by a fast intensified camera. Several cameras have been

Table 1. Experimental configurations list

nozzle nominal Mach	matched p_0/p_a ratio	Mach range	experimental and numerical domain		vessel configuration
			width \times length [nozzle output radii r_n]	[initial jet radii r_0]	
10	6.667×10^3	7.5 to 12.5	$41.7 \times 210.$	$62.0 \times 310.$	3 sections (2.48m)
15	4.762×10^4	13.5 to 17	$14.0 \times 70.$	$32.0 \times 165.$	3 sections (2.39m)
20	1.786×10^5	17.5 to 21	$8.20 \times 50.$	$24.9 \times 149.$	full length (3.28m)

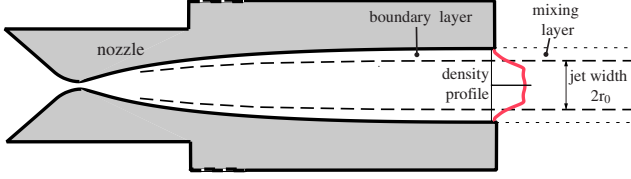
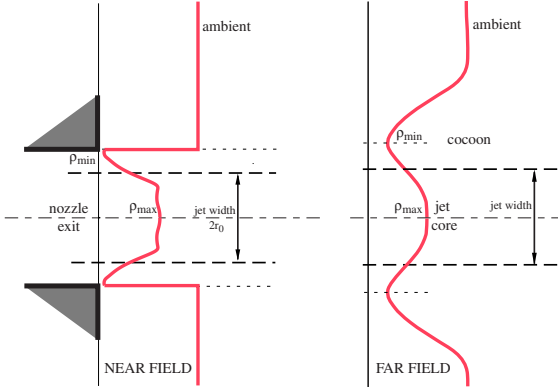
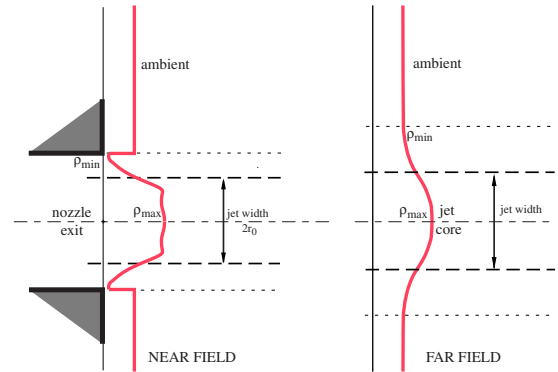
**UNDERDENSE JET****OVERDENSE JET**

Fig. 2. Output density curve and actual jet width under matched conditions. Upper panel: density and jet sketch at the output of the Mach 10 nozzle. Mid panel: density profiles and jet widths in the near and far fields for an underdense jet. Lower panel: density profiles and jet widths in the near and far fields for an overdense jet

tested and used up to now, reaching speeds up to 8100 frames per second (fps). The image resolution is typically 512×512 . The most performant camera in use acquires these images by means of a 32×20 mm CMOS sensor that receives light

from an intensifier having a sensitive photocathode with a diameter of 25 mm. The time exposure is forced by the extreme conditions of this experiment where two opposite needs must be balanced, namely a short exposure to obtain sharp images and a long exposure to obtain a sufficient light level. In general, it is selected the longest exposure compatible with the frame rate, i.e. the inverse of the frame rate minus the readout time. For example, at 8100 fps the exposure is $122.3 \mu\text{s}$, at 4000 fps it is $248.9 \mu\text{s}$. Since phenomena taking place over much shorter times are unavoidably blurred by the system, these time values can be considered close to the temporal resolution. The spatial resolution instead can be quantified reporting the visible jet width in pixels of the original images, this value ranges approximately from 30 to 100 and it can be easily converted in a mm value by the optical magnifying factor. This factor depends on the specific setup for each experimental session. However, in general it is of the order of the unity. The movies obtained by this system contain a number of useful frames which is different for each test, this number varies approximately from 25 for the fastest jets to more than 150 for the slowest ones.

Besides visualizations, flow structure velocities and gas densities can be measured through image processing. Measurements of velocities can be obtained by special correlation techniques, applied to the typical macroscopic structures appearing in the jet morphology, such as the head bow shock, secondary moving shocks or expansions and mixing layers instabilities. A detailed description of the correlation techniques in use cannot find place in this work, see for example Tordella et al. (2011). However, here the main keypoints are synthesized. Considering two consecutive frames as monochromatic pixel matrices A_{ij} and B_{ij} , and extracting two rows a_j and b_j containing the information about the moving structure, the displacement of this structure is obtained by calculating a correlation product of the kind

$$h_k = \sum_j [a_j \cup R(b_j)][b_{k+j} \cup R(a_{k+j})],$$

where R is a reflection operator that reverses the order of the elements in a pixel row. The resulting vector h_k , that can also be expressed as a convolution product, has a maximum at $k_{max} = s$, where

s (in pixels) is the structure shift between the two images. Then, dividing by the interframe time, the s/t ratio becomes a measure of the structure velocity. When this velocity is known, two consecutive images containing the same structure can be juxtaposed after shifting the second one by s pixels. This procedure can be repeated making use of different velocity measurements (head velocity, instability waves...), leading to partial reconstructions of the jet morphology, consisting of juxtaposed parts ('slices') of adjacent frames. Of course, this kind of reconstruction has a physical meaning only if the changes in the structure properties are slow compared to the interframe time, so that it cannot be performed over an arbitrarily large number of frames, in order to avoid a 'frozen' representation of the flow under test. For these reasons, the presented results have been obtained by juxtaposing small numbers of slices (less than 15) coming from wide frames (about 0.4m each) obtained by wide angle lenses.

Density measurements in extended spatial regions are possible due to the proportionality between gas density and light intensity in the working pressure range. In fact, the working conditions in the vacuum vessel permit the use of the well-known relation

$$I = k_g \rho, \quad (1)$$

where I is the light intensity taken from a sub-region of the image and k_g is a constant relevant to the tested gas (Brown and Miller 1957, Muntz 1968, Bütetfisch and Vennemann 1974). The constant k_g is obtained from direct calibrations performed on each tested gas (Belan et al. 2008).

3. Numerical setup

We have solved numerically the hydrodynamic ideal equations Eqs. 1, 2, and 3 (Sect. 5). The simulations have been carried out on a 2D domain in cylindrical coordinates (r, z) , which are normalized over the initial jet effective radius r_0 (Fig. 2). The z axis represents the longitudinal direction of the jet. Due to the axial symmetry of the problem, we will consider a domain going from $r = 0$ to $r = R_{\text{vessel}}$.

The domain chosen depends on the nominal jet Mach number considered: for the cases with the $M = 10$ nozzle we have assumed a domain of $31 \times 310 r_0$ including 128×1280 zones; for the cases with the $M = 15$ nozzle the domain was $16.5 \times 165 r_0$ with the same number of grid zones; for the cases with the $M = 20$ nozzle we had $12.5 \times 150 r_0$ including 128×1500 zones. Exploiting the axial symmetry, the domains chosen for carrying out the numerical calculations are the half of the ones reported in Table 1.

We have imposed reflective boundary condition on the axis of the jet and at $z = z_{\text{vessel}}$. At $r = R_{\text{vessel}}$ we have

imposed that the flow velocity must be zero. We have verified that this condition mimics the experimental behavior at best. The jet was injected at the boundary $z = 0$ and the temporal dependence of the physical quantities was carefully modeled (Tordella et al. 2011).

We employed the PLUTO numerical code by Mignone et al. (2007) (<http://plutocode.ph.unito.it/>) for the solution of hypersonic flows. The code provides a multiphysics, multialgorithm modular environment which is particularly oriented towards the treatment of astrophysical flows in the presence of discontinuities. Different modules and algorithms may be independently selected to properly describe Newtonian, relativistic, MHD, or relativistic MHD fluids. In this case, Newtonian ideal hydrodynamics has been used. This module exploits a general framework to integrate a system of conservation laws, built on modern Godunov-type shock-capturing schemes.

4. Results

A large set of jets has been studied in the experimental investigation. The Mach numbers range from 7 to 21, and the density ratio η from 0.5 to more than 100. For a number of jets, also the corresponding numerical simulations have been realized.

4.1. Morphologies

This section presents the different morphologies observed at some significant density ratios and Mach numbers, selected as follows: Figs. 3 to 5 show 3 sets of jets, chosen in order to present slightly underdense, slightly overdense and overdense jets. For each set, 3 different Mach numbers are selected, and for each jet the laboratory visualization is compared with the numerical simulation. In the visualizations, thanks to the electron beam technique, the light intensity is proportional to the local density, whereas in the corresponding numerical simulations the density maps are intentionally produced **for the sake of comparison with the experiment, even if the simulations may easily produce maps for many other quantities.**

Each experimental image is obtained by juxtaposition of time-correlated frames on a short time range including the instant chosen for the corresponding numerical image, **as explained in Section 2. This kind of treatment has been introduced because of the limitation in size of the optical window in the experiment (Fig. 1), that even by using wide angle lenses cannot be larger than about 0.4m. So doing we extend the jet image over a wider spatial range than that seen in a single camera frame, but limiting the number of frames in order to maintain the right physical meaning of these reconstructions.** The resulting image is then compared to the corresponding numerical simulation, which is inherently a fixed-time representation of the same phenomenon over the complete spatial domain.

Fig. 3 shows 3 light, underdense jets, having similar density ratios < 1 and Mach numbers from 10 to 18.

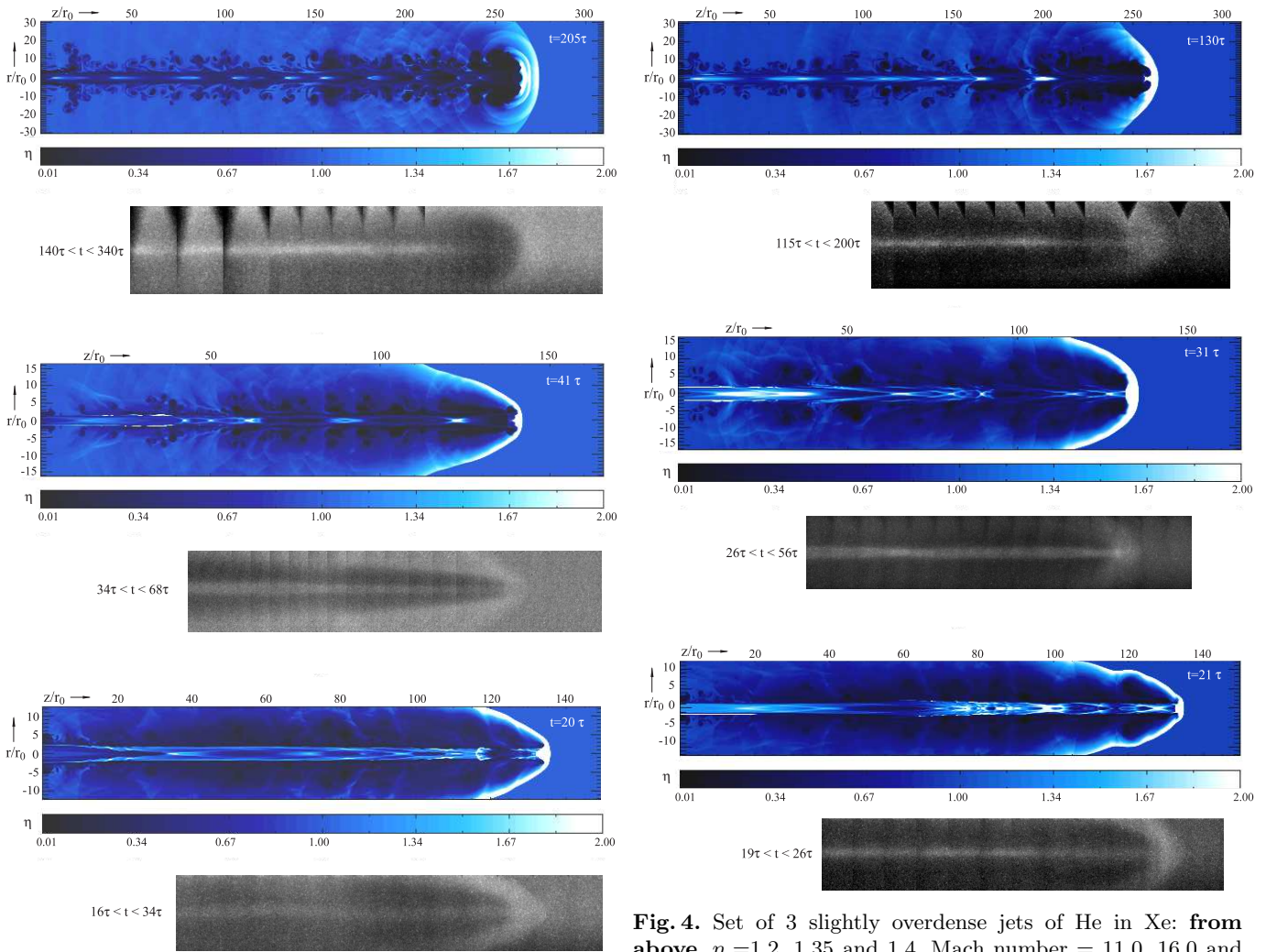


Fig. 3. Set of 3 slightly underdense jets of He in Xe: **from above**, $\eta = 0.85, 0.9$ and 0.9 , Mach number = 10.0, 13.5 and 18.0. Length is expressed in r_0 units (effective or reference jet radius) and time in τ units, i.e sound crossing time over jet radius. The numerical density scale is referred to the unperturbed ambient density.

Many known properties are visible both in the experiments and in the simulations, namely the presence of a large cocoon, the **possible appearance** of compression knots along the jet core and the increasing bluntness of the jet head for decreasing Mach numbers. However, the last property must be considered by keeping in mind that head shape changes continuously with time, owing to the beam pumping phenomenon (Kössl and Müller 1988, Massaglia et al. 1996, Tordella et al. 2011). **In fact, as the hypersonic material at the jet head interacts with the ambient forms a strong shock (called *Mach disk*). The back-flowing, shocked jet material inflates an expanding overpressured region called *cocoon*, that in turns squeezes the jet and drives shock waves into it, which on the axis assume the characteristic biconical shape. These shocks modify the struc-**

Fig. 4. Set of 3 slightly overdense jets of He in Xe: **from above**, $\eta = 1.2, 1.35$ and 1.4 , Mach number = 11.0, 16.0 and 18.0.

ture of the jet head, including the bow shock that precedes the Mach disk, and affect its propagation velocity into the ambient medium. It is also important to note that the experimental observation of the head structure and of the knots is difficult because of the finite, non-negligible exposure time of the camera, which is necessary for getting enough light. This produces an unavoidable image blur effect since the displacement of the structures under study is not always negligible during a typical exposure time. This effect is also discussed in Section 4.2.

A simple quantitative comparison between experiments and simulations can be made by measuring the jet head velocity V_{exp} . The results are in Table 2 and show a good agreement with the numerical results V_{num} , slightly worsening at the lowest Mach number. For the experimental images, the results have been obtained by means of the above mentioned correlation technique. **In this and in the following tables, the accuracy reported for the simulated velocity is mainly due to the errors introduced by setting the accessory**

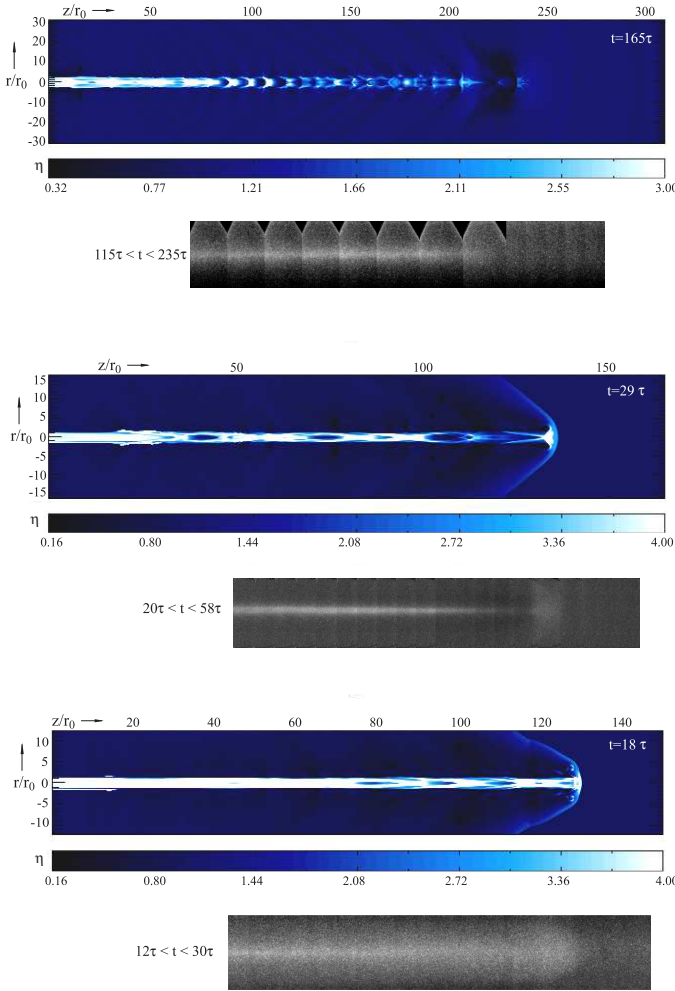


Fig. 5. Set of 3 overdense jets of He: **from above**, ambient is air, air, He, $\eta = 4.4, 4.6$ and 5.4 , Mach number = $7.0, 14.3, 17.9$.

conditions of the simulations in such a way as to reproduce the experimental cases under test. The inherent accuracy of the PLUTO code instead is several orders of magnitude better than the experimental one. In the laboratory image at Mach 18, see Fig. 3, one can see a non-axially symmetric displacement of the jet core, which cannot be reproduced in the related two-dimensional axisymmetric numerical simulation (**lower panel**). This property must be numerically investigated by considering a three-dimensional domain in further studies. At the moment, we might interpret this observation as an effect of the higher Reynolds number at the nozzle exit that disrupts the symmetry of the mean base flow. In particular, one must consider the effects associated to the viscous and turbulent boundary layer developing along the inner surface of the long de Laval nozzle necessary to generate the Mach 20 jets (see Fig. 1). This long layer can act as a source of excitation for the long transversal perturbation observed in this image. However, whether this behavior at high Mach numbers is an effect

of the injection mechanism adopted or is the result of the growth of intrinsic non-axially symmetric jet modes remains to be investigated.

Table 2. Head velocities for Fig. 3

Mach	η	V_{exp} [m/s], $\pm 20\%$	V_{num} [m/s], $\pm 7\%$
10.0	0.85	155	200
13.5	0.9	340	350
18.0	0.9	645	750

Fig. 4 shows 3 slightly overdense jets, having similar density ratios > 1 and Mach numbers from 11 to 18. Again, both in the experiments and in the simulations a cocoon and some compression knots are visible, whereas the jet head is blunter for lower Mach numbers. With respect to the underdense jets, here the higher density ratio causes a slight decrease of the cocoon and jet head sizes. The comparison between experimental and numerical jet head velocities is shown in Table 3, also in this case the agreement is fair, worsening at the highest Mach number.

Table 3. Head velocities for Fig. 4

Mach	η	V_{exp} [m/s], $\pm 20\%$	V_{num} [m/s], $\pm 7\%$
11.0	1.2	335	340
16.0	1.35	490	500
18.0	1.4	415	550

Fig. 5 shows 3 overdense jets, having similar density ratios ~ 5 and Mach numbers from 7 to 17.9. **Unlike the previous cases, where He jets travel in Xe ambients, here the He jets travel in different ambients, made of air or He, a necessary choice in order to obtain the desired density ratios, as explained in Section 2.** The presence of a different ambient gas does not prevent the comparison with the previous cases since the ambient is not accelerated so much as to introduce secondary effects due, for example, to the molecular structure of the ambient gas. In this case, as expected, the backward flow zone related to the cocoon formation has a definitely smaller size and the compression zones, when present, are narrowly spaced, so that they cannot be resolved by the experimental technique. The jet head structure is smaller than in the previous cases – it must not be confused with the bow shock, which reaches the boundaries of the domain. **Unfortunately, at the lowest Mach number presented in this figure, the formation of a proper head structure is hampered by the pressure ratio p_j/p_a which in this particular case turns out to be 0.77, i.e. at the very limit of the value allowed for a nearly matched condition.** The comparison between experimental and numerical jet head velocities is shown in Table 4, excluding the lowest

Mach number jet for the reasons mentioned above, even in this case there is a good agreement.

Table 4. Head velocities for Fig. 5

Mach	η	V_{exp} [m/s], $\pm 20\%$	V_{num} [m/s], $\pm 7\%$
14.3	4.6	580	600
17.9	5.4	680	700

It is worth noting that pressure matched hypersonic hydrodynamic jets maintain their collimation up to large distances from the launching region, at least within the physical limits of the walls of the chamber. One must note however that these jets are undisturbed in their propagation, apart the self-induced non-axisymmetric long wave instability seen in the case of the underdense jet at Mach number 18 and Reynolds number $\sim 10^5$, see discussion above. It would be interesting, also from the astrophysical point of view, to modify the experimental setup for inducing some controlled non-axial perturbation in the flow at the nozzle exit, in particular to understand which part of the evolution is much influenced by the boundary condition at the nozzle.

4.2. Effects of the exposure time

In Fig. 6 we show what one obtains when the effect of the finite experimental exposure time is taken into account in the simulated density distribution. This figure has been created by superimposing density maps taken in a time interval of the order of the exposure time, so that at each point the density has a time-averaged value. The case under test is the He jet in Xe ambient at the center of Fig. 4 ($\eta = 1.35$ and $M = 16.0$): one can see that the simulated density map of Fig. 6 is more similar to the experimental image than the original simulation, which is a instantaneous representation of the field. **The time interval used to create this density map, $28\tau < t < 33\tau$, is of the order of the exposure time, and must not be confused with the time interval $26\tau < t < 56\tau$ used to extract and juxtapose frames from the movie, which is definitely larger for the sake of comparison with numerical images.** Another minor reason for blur, however, cannot be accounted for in Fig. 6, and it is due to the finite time needed for the excitation of molecules by the electron beam, so that the light emission is delayed while they drift downstream of the excitation point.

4.3. Density measurements

Another kind of quantitative result is given in Fig. 7, where the proportionality law (4.3) between the fluorescent light intensity and the gas density is used to measure density values along the axes of the 3 slightly overdense jets of Fig. 4. The propor-

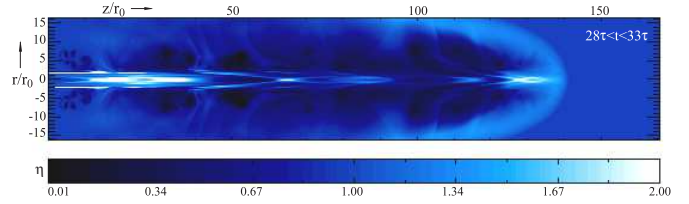


Fig. 6. Simulation of the overdense jet at center of Fig. 4 (Mach number = 16) obtained by averaged superposition of density maps over a time interval of the order of the experimental image exposure.

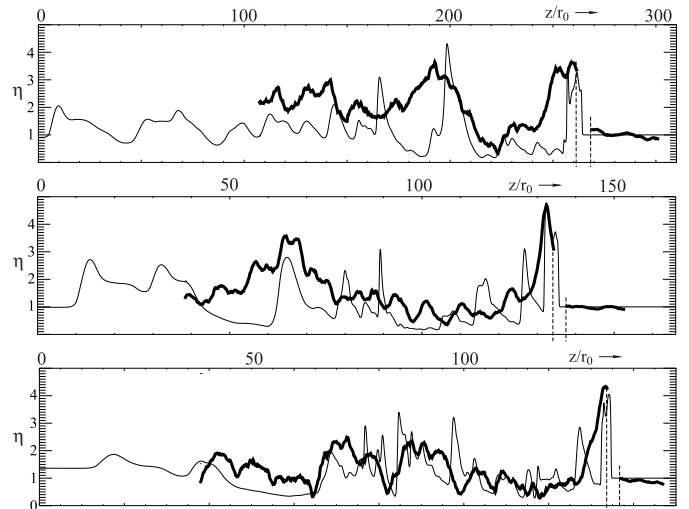


Fig. 7. Numerical (thin lines) and experimental (thick lines) axial densities for the 3 slightly overdense jets of Fig. 4. Densities are expressed in nondimensional form as density ratios η referred to the unperturbed ambient. **The space between vertical dashed lines is a non-measurable zone, see the text, Section 4.3.**

tionality constant for each gas species is known by calibration. Whenever possible, the results are obtained by using different values of this constant for different gas species (the inner zone of the jet heads, namely the region between the bow shock and the terminal shock or Mach disk, cannot be analyzed because it contains two mixed gas species, **it is represented in Fig. 7 as an empty space between vertical dashed lines**). The output density values are corrected accounting for the image background noise and the final curves are compared with the relevant numerical ones. The results, given in terms of the density ratio η referred to the unperturbed ambient, show that the experimental technique is capable to reproduce the large scale density variations, whereas the small scale details are lost. However, it must be recalled that the small scale structures exhibit turbulent temporal variations scarcely reproducible. That is, even a higher time resolution of the camera producing less blur in the experimental images would probably reveal different small scale variations at each repetition of the same jet.

Table 5. Physical parameters for the laboratory Helium jets

Case	η	Mach	p_j [Pa]	$\rho_j \times 10^{-4}$ [Kg m $^{-3}$]	V_j [m s $^{-1}$]	t_j [ms]	τ [ms]
Fig.3, top	0.85	10.	5.0	2.1	2000	15.	0.042
Fig.3, mid.	0.85	13.5	9.5	6.9	2050	8.6	0.10
Fig.3, bot.	0.9	18.	4.0	4.1	2300	5.3	0.18
Fig.4, top	1.2	11.	3.5	1.7	2040	8.8	0.062
Fig.4, mid.	1.35	16.	4.0	2.9	2420	6.0	0.090
Fig.4, bot.	1.35	18.	2.5	2.0	2600	7.3	0.26
Fig.5, mid.	4.6	14.3	14.	7.6	2510	5.0	0.10
Fig.5, bot.	5.4	17.9	2.5	2.7	2220	6.0	0.18

5. Discussion

The ideal hydrodynamic equations, in absence of dissipation effects and radiative cooling, can be written as:

$$\frac{\partial \rho}{\partial t} + \nabla \cdot (\rho \mathbf{v}) = 0 \quad (2)$$

$$\rho \left(\frac{\partial}{\partial t} + \mathbf{v} \cdot \nabla \right) \mathbf{v} = -\nabla p \quad (3)$$

$$\frac{\partial p}{\partial t} + (\mathbf{v} \cdot \nabla) p - \gamma \frac{p}{\rho} \left(\frac{\partial}{\partial t} + \mathbf{v} \cdot \nabla \right) \rho = 0 \quad (4)$$

where \mathbf{v} , p and ρ are the fluid velocity, pressure and density and γ is the ratio of specific heats. These equations are invariant under the transformation (Ryutov et al. 1999):

$$r = a r_1, \quad \rho = b \rho_1, \quad p = c p_1, \quad t = a \sqrt{\frac{b}{c}} t_1, \quad \mathbf{v} = \sqrt{\frac{c}{b}} \mathbf{v}_1 \quad (5)$$

where a , b and c are arbitrary positive numbers (“Euler similarity”).

For applying the Euler similarity, the system must have large Reynolds and Peclet numbers (Re and Pe) with respect to the unity and small localization parameter (K or Knudsen number, the ratio of the collisional mean-free-path to the typical scale length of the system). We recall the definitions for these parameters:

$$Re = \frac{\nu r_0}{\nu}, \quad Pe = \frac{\nu c_p r_0}{\kappa}, \quad K = \frac{\lambda}{r_0}, \quad (6)$$

where ν is the kinematic viscosity, c_p the heat capacity, κ the thermal conductivity, λ the collisional mean-free-path and ρ the mass density, and where we have taken the radius r_0 as typical scale of the system.

For verifying whether the hypersonic flows generated in the laboratory are Euler similar to YSO jets we recall some “fiducial” values of length, density and pressure of the astrophysical objects (Teşileanu et al. 2012): jet radius $\tilde{r}_j = 20 \text{ AU} = 3 \times 10^{12} \text{ m}$, temperature $\tilde{T}_j = 2500 \text{ K}$ and particle density (mostly Hydrogen) $\tilde{n}_j = 10^{10} \text{ m}^{-3}$, thus the mass density results $\sim 10^{-17} \text{ Kg m}^{-3}$. The pressure can then be obtained by the ideal gas law as $\sim 3 \times 10^{-10} \text{ Pa}$. **As reported in Section 1, observational data include Mach numbers approximately ranging from 10 to 40 and density ratios from 1 to 10.**

The corresponding values for laboratory flows can be essentially expressed by the effective radius range $8 \times 10^{-3} < r_0 < 22 \times 10^{-3} \text{ m}$, the Mach number range $7 < M < 18$ and the density ratio range $0.85 < \eta < 5.4$. Temperatures, densities and pressures are respectively in the order of $\sim 10 \text{ K}$, $\sim 10^{-4} \text{ Kg m}^{-3}$, $\sim 5 \text{ Pa}$. The Reynolds number of the experimental flows is of the order of 10^4 for the jets issuing from the Mach 10 nozzle, and of the order of (or larger than) 10^5 for the higher Mach nozzles, while the Peclet Number is $Pe \sim 10^2 - 10^3$. The Knudsen number turns out to be $K \sim 10^{-3} - 10^{-2}$. It is interesting to note that, in the case of YSO jets, the values for Re and Pe are huge and K attains as well values $\sim 10^{-2} - 10^{-3}$. This confirms that the ideal Euler equations Eqs. 1, 2, 3 are a good description of the dynamics of the flows under discussion.

We can now estimate the constants a , b and c (Eq. 5) and, given the gas velocities and evolution times, derive the similarity values for YSO jets. In this case, r , ρ and p correspond to the astrophysical values \tilde{r}_j , $\tilde{\rho}_j$ and \tilde{p}_j while r_1 , ρ_1 and p_1 correspond to the laboratory values of r_0 , ρ_j and p_j listed in Table 5. The values for jet flow velocity V_j , on-axis and at nozzle output, are listed in Table 5 as well. The flow velocity is simply derived from the relation $V_j = \sqrt{\gamma p_j / \rho_j}$. We recall that the elapsed time t_j is the time for the jet head to reach the end of the vessel. **The last column reports also the time scale of the jets (sound crossing time over radius).**

The results for the Euler similar, scaled values are listed in Table 6. We see that the values for the jet velocities V_{ES} range between 80 to about 140 km s^{-1} and the scaled times t_{ES} considered between about 400 up to 5,000 years. We recall that YSO jets velocities are typically in the range $\sim 100 - 400 \text{ km s}^{-1}$ and their lifetime lasts $\sim 10^4 - 10^5 \text{ ys}$. Thus the values for the velocities are close to the actual observed values for “slow” YSO jets, while the simulated times cover a sizable fraction of the life-span of the astrophysical objects.

6. Conclusions

The experimental facility and instrumentation has shown to fit the experimental requirements and to give valid results for the aim it was designed and assembled. Both

Table 6. Euler similar, scaled physical parameters for the laboratory Helium jets

Case	t_{ES} [ys]	V_{ES} [km s ⁻¹]
Fig.3, top	4950	77
Fig.3, mid.	1150	103
Fig.3, bot.	400	138
Fig.4, top	2700	84
Fig.4, mid.	800	122
Fig.4, bot.	650	138
Fig.5, top	750	109
Fig.5, mid.	450	136

experiments and numerical simulations have shown detailed aspects of the head bow shock, its bluntness versus Mach number and the shape of the cocoon as function of the density ratio. In this sense the use of gases of strong density difference, as Helium and Xenon has been of focal importance. We note that both the experiments and the numerical simulations are in good agreement in most cases. Moreover, the Euler similar scaled flows that we reproduce in the laboratory are characterized by velocities also in good agreement with YSO jets values. The physical characteristics of simulated jets, i.e. head and jet velocities, bow-shock and cocoon morphologies, that we discuss in the paper, are intentionally limited to the ones that can be obtained either by direct measurements or derived in the laboratory experiments and thus subjects of comparisons. These ones suggest once again that the PLUTO code may be considered a valid tool for HD simulations of astrophysical jets, as useful tool for further investigations. **Physical ingredients, such as radiative cooling and magnetic fields, that are of utmost importance in determining the jet emission details, the former one, and the outflow launching, the latter one, are absent in our investigation. However, we can say that the basic features of the jet dynamics are well described by the HD treatment alone, and is therefore reasonable to assume that fluid dynamics may explain the major facets of the behaviour of YSO gas jets as far as the morphology and collimation are concerned.**

About the experiments, we are almost at the limits of the instrumentation capabilities: it is difficult to imagine to have cameras with higher performance in resolution or sensitivity and acquisition time or to increase the electron beam characteristics of current beyond 2 mA without increasing the beam width, or voltage, going into X-ray emission. **A significant change could be achieved by using different measurements techniques, like molecular tagging velocimetry or laser interferometry, of course these techniques should be considered as radical, long term modifications of the existing setup.** Another progress in the facility is to further heat the gas jet, a thing that will require major modifications to the full system, which now has the advantage to

be a manageable low energy facility, and that will require to afford a rather high cost.

Acknowledgements. The authors wish to thank Andrea Milanese of the LA.S.T. laboratory (Politecnico di Milano). They also thank an anonymous referee whose careful comments have helped to improve the paper.

References

- Ashkenas, H. & Sherman F.S., in 'Rarefied gas dynamics', edited by deLeeuw J.A., Academic, NY, 1966
- Belan M., De Ponte S., Tordella D. 2008, *Exp. Fluids*, 45, 501
- Belan M., De Ponte S., Tordella D., 2010, *Phys. Rev. E*, 82, 026303
- Belan M., De Ponte S., Tordella D., Massaglia S., et al., 2011, *Ap&SS*, 336, No.1, 9-14
- Belan M., Mirzaei M., De Ponte S., Tordella D. 2012, *EPJ Web of Conferences* 25, 01056
- Bellan, P. M., You, S., Hsu, S. C. 2005, *Ap&SS*, 298, 203
- Bellan, P. M., Livio, M., Kato, et al., 2009 *Phys. Plasmas*, 16, 4
- Brown, L. O. and Miller N. 1957, *Trans. Faraday Soc.* 53: 748
- Bülent Yüceil K., Volkan Ötügen M. 2002, *Phys. Fluids* 14, 4206.
- Bütfisch K.A., Vennemann D. 1974, *Prog Aer Sci* 15: 217–255.
- Ciardi, A., Lebedev, S. V., Frank, A., et al., 2009, *ApJ*, 691, L147
- Falize, É., Michaut, C., Bouquet, S., 2011, *ApJ*, 730, 96
- Fender, R., 2004, *ARAA*, 42, 317
- Frank, A., *Asymmetric Planetary Nebulae 5 conference*, Bowness-on-Windermere, U.K., 20 - 25 June 2010, A. A. Zijlstra, F. Lykou, I. McDonald, and E. Lagadec, eds. (2011) Jodrell Bank Centre for Astrophysics
- González, M., Audit, E., Stehlé, C., A & A, 2009 497, 27
- Granot, J., 2007, *RevMexAA (Serie de Conferencias)*, 27, 140-165
- Gregory, C. D., Howe, J., Louprias, B., Myers, S., and 9 coauthors, 2009, *Ap&SS*, 322, 37
- Hartigan, P., Foster, J. M., Wilde, B. H., et al., 2009, *ApJ*, 705, 1073
- Hester, J. J., *ARAA*, 2008, 46, 127
- Kössl, D., Müller, E., A & A, 1988 206, 204
- Lebedev, S. V., Ampleford, D. J., Ciardi, A., et al. 2004, *ApJ*, 616, 988
- Lebedev, S. V., Ciardi, A., Ampleford, D. J., et al. 2005, *MNRAS*, 361, 97
- Love, E.S., Grigsby, C., Lee, L. & Woodling, M. 1959, *NASA Tech. rep. TR R-6*
- Massaglia, S., Trussoni, E., Bodo, G., Rossi, P., Ferrari, A., 1992 *A&A* 260, 243
- Massaglia, S., Bodo, G., Ferrari A., 1996 *A&A*, 307, 997
- Micono, M., Bodo, G., Massaglia, S., Rossi, P., Ferrari, A., Rosner, R., 2000, *A&A* 360, 795
- Mignone A, Bodo G, Massaglia S, et al., Matsakos G, Tesileanu O, Zanni C and Ferrari A 2007, *ApJS*, 170, 228
- Muntz E. P. 1968, *AGARDograph* 132.
- Norman, M. L., Winkler, K.-H. A., Smarr, L., Smith, M. D., 1982, *A&A*, 113, 285
- Reipurth, B., Bally, J., 2001, *ARAA*, 39, 403
- Rus, B., Mocek, T., Prag, A.R. et al., 2002, *PRA* 66, 063806
- D. Ryutov, R. P. Drake, J. Kane, E. Liang, B. A. Remington, W. M. Wood-vasey 1999, *ApJ*, 518,821

- Suzuki-Vidal, F., Hall, G.N., Bland, S.N., et al., 2010, Phys. Plasmas, 17, 112708
- Teşileanu, O., Mignone, A., Massaglia, S., Bacciotti, F., 2012, ApJ 746, 96
- Tordella D., Belan M., Massaglia S., et al., 2011, NJP, 13, 043011
- Tzeferacos P. Ferrari, A., Mignone, A. et al., 2009, MNRAS, 400, 820
- Zaman K. B. M. Q. 1998, Phys. Fluids 10, 2652.
- Zaman K. B. M. Q. 1999, J. Fluid Mech. 383, 197